NMR and ESR relaxation in Nd- and Gd-doped LaPO4 : towards the accurate determination of the doping concentration

Sébastien Maron, Géraldine Dantelle, Thierry Gacoin, François Devreux

NMR and ESR Relaxation in Nd- and Gd- doped $LaPO_4$: Towards the Accurate Determination of Doping Concentration

Sébastien Maron[1], Géraldine Dantelle[1,2], Thierry Gacoin, François Devreux

Physique de la Matière Condensée
École Polytechnique - CNRS
91128 Palaiseau Cedex, France

[1] corresponding author: sebastien.maron@polytechnique.edu
geraldine.dantelle@polytechnique.edu
[2] present address: Institut Néel, 25 avenue des Martyrs, 38 042 Grenoble Cedex, France

Abstract: We present an original method based on the ^{31}P solid-state NMR relaxation to determine low concentrations (< 1 at.%) of paramagnetic ions in monazite $LaPO_4$ crystals with a high accuracy (~ 0.1 at.%). NMR experiments in static and MAS (15 kHz) conditions show that the ^{31}P relaxation time T_1 is strongly affected by the presence of paramagnetic ions in the vicinity of the phosphorous nuclei. A linear variation of $1/T_1$ as a function of Nd^{3+} or Gd^{3+} concentration is shown in the 0-10 at.% range for a homogeneous distribution of the doping ions in the matrix, which is the case when doped $LaPO_4$ is synthesized by a soft chemistry route, *i.e.* by aqueous coprecipitation followed by thermal annealing. As a proof of concept for the use of this tool to study dopant homogeneity, we show that in the case of a solid-state synthesis at 1350 °C, relaxation measurements show that the homogeneous distribution of the doping ions is ensured when the mixing of the oxide precursors is performed mechanically, but not in the case of a manual grinding. The electronic relaxation times of Gd^{3+} and Nd^{3+} ions are evaluated by ESR measurements under saturation conditions. This allows us to provide a semi-quantitative interpretation of the nuclear ^{31}P relaxation measurements both in Nd and Gd doped $LaPO_4$. In addition, the comparison between nuclear and electronic relaxation suggests that Nd-Gd codoping may improve the efficiency of the Gd^{3+} ion as relaxing agent in MRI (Magnetic Resonance Imaging) techniques.

1. Introduction

In many cases, specific properties are conferred to oxide materials by the substitution of one ion forming the network by another ion with interesting optical or magnetic characteristics. It is the basic principle used for the synthesis of laser materials ($Al_2O_3:Ti^{3+}$, $YAG:Nd^{3+}$…), of materials for displays ($BaMgAl_{10}O_{17}:Eu^{2+}$ [1]…), of materials for lighting devices ($YAG:Ce^{3+}$ [2], $Ba_9Y_2Si_6O_{24}:Ce^{3+}$ [3]), *etc*. In cases where the doping ion has the same size and charge as the substituted ion, the substitution can be done in the whole range of concentration (total solid solution). It is for example the case of $Y_2O_3:Eu^{3+}$, also labelled $Y_{2-2x}Eu_{2x}O_3$, where x can vary continuously from 0 to 1. However, it is often essential to limit the doping concentration since the physical properties can be affected at high doping level, *i.e.* when the distance between active ions is small, typically of the order of a few nm. In the case of luminescence properties, high doping concentrations often induce a reduction of luminescence by concentration quenching due to energy transfers between doping ions [4,5]. In a large number of materials, the doping concentration is nevertheless limited to a few at.% as a result of limited solid solution range [6]. In this case, approaching the highest concentration often leads to clusters of dopant ions. Such clustering can also lead to concentration quenching due to the small distance between doping ions within the clusters [7]. In addition, we could also note that in the case of nanostructured materials, it is difficult to distinguish between adsorbed ions and ions incorporated in solid solution.

In order to obtain structural information and get a better understanding of the substitution mechanisms, it is a real challenge to know precisely the doping concentration, especially for weak doping concentrations (typically < 5 at.%). Moreover, the control of the concentration and homogeneity of the doping species in a given matrix is a basic requirement for the control and optimization of optical and magnetic properties of materials.

Different techniques are frequently used to gain insights into the doping concentration and homogeneity. The most common one consists in determining the unit cell parameters of undoped and doped compounds using powder X-ray diffraction, and then in deducing doping concentration by assuming a linear variation of the unit cell parameters with the doping concentration according to the Vegard's law [8]. Though largely used, this technique is not accurate for the determination of weak doping concentrations and we can estimate its precision at ~ 1 at.% for doping concentrations smaller than 5 at.%. Moreover, it does not allow detecting the presence of small clusters since the unit cell parameters are averaged on the whole sample. Another technique relies on the Energy Dispersive X-ray (EDX) analysis, which allows identifying the elemental composition of materials. In a standard TEM, its

precision, which depends on the elements, is not better than ~ 1 at.%. The presence of clusters is hardly detectable since the measurements are averaged over ~ 1 μm^2. However, EDX analyses drawn from High-Angle Annular Dark-Field images made by Scanning Transmission Electron Microcropy (HAADF-STEM) can visualize clusters thanks to a Z^2 contrast, with Z being the atomic number [9]. This technique is efficient for the determination of local segregations, but it remains limited to probe a significant sample volume and get a macroscopic estimation. Finally, in the case of the doping by paramagnetic ions, Electron Spin Resonance (ESR) can be used to quantify the proportion of doping ions and to observe the formation of clusters. Using a calibrated sample, it is possible to determine small doping concentrations, but the precision is estimated to be not better than 15%. The advantage of this technique is that the presence of small paramagnetic clusters can also be ascertained [10]. However, if this technique is very efficient in single-crystals where ion pairs can be precisely described [11], it is not applicable in polycrystalline samples nor in glasses where the wide distribution of the electron spin orientations broadens the EPR signal [12].

Hence, taking into account the drawbacks of the different methods described above, we investigate here the possibility of using the solid-state nuclear relaxation to determine low concentrations of paramagnetic ions in diamagnetic matrices with high accuracy (< 0.1 at.%). Solid-state Nuclear Magnetic Resonance (NMR) has been widely used to study the presence and the distribution of doping ions in a diamagnetic matrix by studying the resonance shift induced by the presence of one or more paramagnetic ions in the vicinity of the observed nuclei [13,14]. Here we use the variation of the nuclear relaxation time T_1 as a function of the number of paramagnetic ions in their vicinity in order to quantify the paramagnetic ion concentration and its homogeneity. This strategy is original and, to our knowledge, was only reported by S. Sen and J. F. Stebbins [15,16] in glasses and more recently by E. M. Levin *et al.* [17] in semi-conductors. In respect to these previous works, our goal is to demonstrate the universality of the technique and to study its potentiality as a tool to determine doping concentration and homogeneity.

To demonstrate the validity of our approach, we chose to study the $LaPO_4$ matrix doped with paramagnetic lanthanide ions. It is considered as a model system since $LaPO_4$ is known to incorporate continuously lanthanide ions and to form complete solid solutions [18,19,20]. $LaPO_4$ crystallizes either in the rhabdophane structure, which contains water molecules and corresponds to the low temperature phase, or in the monazite structure, which is the high temperature phase. As H_2O molecules act as strong relaxation agents, we considered only the monazite phase, more appropriate for the study of the relaxation of ^{31}P by

the doping ions. Two doping ions, Nd^{3+} ($J = 9/2$, $L = 6$, $S = 3/2$) and Gd^{3+} ($L = 0$, $J = S = 7/2$) were introduced in the $LaPO_4$ matrix in order to show the influence of the electronic properties of the doping ions on the ^{31}P nuclear relaxation time.

In this detailed study, the following questions are addressed: is the doping concentration homogeneous in the $LaPO_4$ monazite matrix? Is the relaxation in solid-state NMR robust to determine with accuracy low doping concentration? In addition, what is the main relaxation channel for ^{31}P nuclei in $LaPO_4$:Nd and $LaPO_4$:Gd compounds?

2. Experimental section

2.1. Sample preparation

Most of the samples were prepared through a coprecipitation route [20]. Rare-Earth (RE = La, Nd and Gd) nitrate precursors (Sigma-Aldrich) were mixed in a Teflon vessel. Pentasodium tripolyphosphate (TPP) was added in excess to the nitrate solution (molar ratio P to RE = 3) in order to stabilize the particles in water . By heating the solution for 3 hours at 90 °C in an oven, the rhabdophane phases, Nd or Gd doped $LaPO_4.nH_2O$ ($n \sim 0.6$), were obtained. After annealing for 4 hours at 1000 °C, the rhabdophane phases were transformed into the dehydrated monazite phases, $La_{1-x}Nd_xPO_4$ or $La_{1-x}Gd_xPO_4$. Co-doped (Gd, Nd) samples were synthesized following the same process.

$LaPO_4$ and $La_{0.99}Nd_{0.01}PO_4$ monazite samples were also directly prepared by the solid-state route using La_2O_3, Nd_2O_3 and $NH_4H_2PO_4$ as precursors [21]. The powders were mixed together in stoichiometric proportions, and then heated at 1000 °C for 2 h for eliminating NH_4. The mixing was performed either manually or using a planetary mill (Fritsch Pulverisette, 20 cycles, corresponding to 5-min grinding at 250 rpm spaced by 30 s pauses). After this first annealing step, the product was mixed again (using the same method, either manually or with a planetary mill) before a second heating at 1350 °C for 8 h to 56 h to obtain the monazite phases.

Finally, a $La_{0.995}Nd_{0.005}PO_4$ sample was made by mixing in equal proportions $LaPO_4$ and $La_{0.99}Nd_{0.01}PO_4$ (obtained by the solid route) either manually or with a planetary mill, and heating the mixture at 1550 °C for 8 hours.

2.2. Structural characterization

Crystallographic view was designed by Vesta software [22]. Powder X-Ray diffraction diagrams of the samples were systematically recorded with an X'Pert Philips diffractometer (40 kV, 40 mA) with CuK_α radiation ($\lambda = 1.54056$ Å). Cell parameters were obtained by

fitting the diffractograms with the software Fullprof [23,24]. The composition of two samples ($La_{0.99}Nd_{0.01}PO_4$ and $La_{0.95}Nd_{0.05}PO_4$) was checked by ICP/MS at the Service Central d'Analyses du CNRS in Vernaison (France).

2.3. NMR

Magic-Angle Spinning (MAS) NMR experiments were performed with a Tecmag spectrometer associated with a 8.48 T Oxford cryomagnet, using a 4 mm MAS Bruker probe either in static conditions or with MAS spinning up to 15 kHz. The ^{31}P Larmor frequency was 145 MHz at this field. H_3PO_4 85% was used as an external reference for chemical shift measurement. Fully relaxed conditions (repetition time of about $5*T_1$) were used for allowing quantitative measurements of the NMR intensities. However, one spectrum was also recorded with a very short repetition time (50 ms) for highlighting the satellite paramagnetic peaks (see section 3.2.1 below). The isotropic peak was determined by varying the rotation speed from 5 to 15 kHz. All spectra intensities were normalized with respect to the mass of the sample and to the number of scans. The spin-lattice relaxation time T_1 was measured by saturation-recovery method, using a sequence of 24 $\pi/2$ pulses (2.1 μs) spaced by 100 ms blanks. The recovery delay was varied from 100 μs and $10*T_1$. The repetition delay of the sequence was 1 s. FIDs were processed with NTNMR (Tecmag) software, applying a line broadening of 50 Hz before Fourier transform. Most of the T_1 experiments were performed with MAS at 15 kHz, and the whole spectrum including sidebands was considered for the relaxation measurements. A few T_1 measurements were also performed in static conditions (see section 3.3.2 below).The software Origin 8.6 was used to determine the magnitude areas of the spectra, and to fit the recovery curves after normalization of the magnetizations to the highest intensity.

2.4. ESR

ESR spectra were recorded using an X-band (9.4 GHz) EMX Bruker spectrometer equipped with an Oxford Helium continuous flux cryostat, allowing to perform the experiments from 4 K to room temperature (RT). The microwave power was varied from 2 μW to 350 mW in order to obtain the saturation curves. A field calibration was performed using an ESR standard, establishing that 0 dB (197 mW) corresponds to 0.11 mT. ESR simulation spectra were made using the software Easyspin [25].

3. Results

3.1. XRD

Both $LaPO_4$ and $NdPO_4$ phases presenting a coherence length of the order of 150 nm are crystallized under the monazite form (monoclinic, $P2_1/n$, Figure 1) after a 4-hour annealing at 1000 °C of the hydrated form (rhabdophane, hexagonal, $P6_222$). Figure 2 shows the variation of the cell parameters of monazite $La_{1-x}Nd_xPO_4$ as a function of x, the Nd doping content. The variations are linear in accordance with the Vegard's law, which indicates a good admixture of Nd^{3+} in substitution to La^{3+} in the $LaPO_4$ matrix. The quantity of incorporated rare earth is confirmed by ICP/MS measurements that gave [Nd]/[La] = 0.011 and 0.049 for two Nd doped samples with $x = 1\%$ and 5%, respectively. In addition, the ICP/MS measurements show an excess of phosphorous with respect to rare-earth ions [P]/[RE] = 1.29 and 1.42 for $x = 1\%$ and 5%, respectively. Such a result was already observed by Lucas *et al.* [26] and can be explained by the excess of phosphorus introduced *via* the TPP reagent. As shown below (section 3.2.1) the phosphorous excess corresponds to phosphate groups tied at the surface of the particles.

3.2. NMR

3.2.1. ^{31}P NMR spectroscopy

The monazite form of $LaPO_4$ presents a main peak at -4.4 ppm (Figure 3a). A broader peak, centered at about -20 ppm is also seen, corresponding to the contribution of another parasitic phase (labelled "AM") similar to the one previously reported in the literature and attributed with not much details to an amorphous phase [13] and represents ~15% of the signal. Considering the process (La:P = 1:3) used for the material synthesis, this phase is expected to arise from phosphate groups at the surface of the particles, since the excess of TPP was intended to stabilize the particles in solution. This was confirmed by the fact that we were able to remove the "AM" peak by working in stoichiometric conditions (La:P = 1:1) or by annealing the sample at 1450°C.

Figure 3b presents a zoom of the NMR spectrum of $La_{0.99}Nd_{0.01}PO_4$ with a short repetition time of 50 ms. This emphasizes the fast relaxing peaks corresponding to ^{31}P having a Nd^{3+} ion in their near environment. They have been quoted A to F, according to the notation by Palke *et al.* [13]. Indeed, the ^{31}P ions with a paramagnetic ion as second nearest neighbor present a paramagnetic shift due to super-exchange interaction through the bonding oxygen. Note that ^{31}P ions with two Nd^{3+} in their near neighbouring would appear at a different positions but their low concentration and their short relaxation time do not allow their observation in these experiments.

Figure 4 displays the MAS-NMR spectra of $La_{1-x}Nd_xPO_4$ with x varying from 0 to 1. The spectra undergo a considerable broadening as the Nd content increases. The isotropic peak is shifted from -4.4 ppm for $LaPO_4$ to about -260 ppm for $NdPO_4$, in agreement with the literature [21]. For the intermediate doping rates, the baseline is not well defined.

Figure 1-SI shows the variation of the normalized intensity of the static NMR signal of $La_{1-x}Nd_xPO_4$ as a function of the Nd content in the range 0 to 10 at.%. One observes that the ^{31}P signal intensity decreases as the paramagnetic ion concentration increases. When fitting the variation by $I(x) = I_0 (1 - n\,x)$, one obtains $n = 6.6$. This means that each Nd^{3+} ion removes 6.6 ^{31}P nuclei from the NMR signal, which is nearly equal to the number (7) of the super-exchange coupled second neighbors.

3.2.2. ^{31}P NMR relaxation

At both low and high Nd concentrations, the nuclear relaxation is approximately exponential, as expected for materials with a homogeneous distribution of doping ions. However, the relaxation profiles are better fitted by a stretched exponential $\exp[-(t/T_1)^{\beta}]$ with an exponent β of the order of $0.8 \sim 0.9$. The departure from the exponential can be explained by the random distribution of the magnetic ions associated with the Magic Angle Spinning. As a matter of fact, MAS is expected to inhibit the secular dipole-dipole coupling that insures a common spin temperature and an exponential relaxation through nuclear spin diffusion. In that case, the through-space dipolar coupling between the nuclear spins and the randomly distributed magnetic ions should give rise to $\beta = 0.5$ [27].This was actually observed for the ^{29}Si relaxation in aluminosilicates containing dilute Fe ions [28]. In our case, the 100% abundance and the high gyromagnetic moment of ^{31}P prevented a complete vanishing of the spin diffusion mechanism. This leads to a value of β intermediate between 1 (homogeneous spin temperature and relaxation) and 0.5 (no spin diffusion). Since the best fitting β values are close from each other for samples with different Nd concentration, we decided to use a common $\beta = 0.83$ to determine T_1 in order to make the comparison of the results for the different samples more consistent.

The variation of the ^{31}P relaxation rate ($1/T_1$) measured with MAS rotation at 15 kHz is displayed in Figure 5 as a function of the Nd content. In the range $x = 0$ to 10 at.% (inset of Figure 5), a well-defined linear variation is observed, in agreement with the recent results obtained by Levin *et al.* in the case of free carriers in thermoelectrics [17,29]. The measured relaxation is dominated by the non-shifted ^{31}P at low Nd concentration, whereas it is controlled by the superexchange coupled ^{31}P at high Nd content. There is a sharp jump of the

relaxation rate around $x = 60\%$. In principle, the transition should appear much earlier, since 48% of the phosphorous nuclei do have at least one magnetic second neighbor as soon as $x = 10\%$ for a fully random distribution. However, their fast relaxation rate, as well as their large frequency shift, reduce their contribution to the MAS relaxation profile. In the transition region, the relaxation is highly non-exponential, highlighting the presence of two contributions. Moreover, the disturbed baseline makes the measurement of the relaxation rate quite difficult in this range of concentration.

Relaxation measurements were also performed on $La_{0.99}Nd_{0.01}PO_4$ after annealing at 1450°C for 4 hours, which leads to the extinction of the "AM" line (see section 3.2.1). The ^{31}P relaxation time was nearly the same as before annealing. This means that the mean distances between the phosphorus nuclei and the magnetic ions are not very different in the monazite phase and in the "AM" phase. However, taking into account the small size of the particles and the low Nd concentration, this does not allow to decide whether Nd ions are present or not in the "AM" phase. The synthesis process leads to favor the hypothesis of the absence of rare earths in the "AM" phase. This may further contribute to explain that the relaxation transition between the "diamagnetic" and "paramagnetic" regions in Figure 5 occurs later than expected.

To prove that the NMR relaxation can be a tool for the study of dopant homogeneity, ^{31}P MAS relaxation measurements were also performed on $La_{0.99}Nd_{0.01}PO_4$ samples prepared by the solid route by mixing powders of La and Nd oxides with the PO_4 precursor [21]. When the grinding of the powders was made manually, the relaxation was strongly non-exponential. A mean relaxation time was measured and was found to be more than twice longer than the one obtained for samples made by coprecipitation (19 s *versus* 8.4 s), whereas it was nearly equal (10 s *versus* 8.4 s) when the grinding was achieved by using a planetary mill. Such a difference was clearly due to the different distributions of the Nd^{3+} ions in the $LaPO_4$ matrix resulting from the mixing processes.

Figure 6 shows the relaxation profiles for two samples resulting from the high-temperature treatment of an equimolar mixture of $LaPO_4$ and $La_{0.99}Nd_{0.01}PO_4$, with the goal of forming $La_{0.995}Nd_{0.005}PO_4$ compounds. Two routes were investigated: $LaPO_4$ and $La_{0.99}Nd_{0.01}PO_4$ were ground, either manually or by using a planetary mill. In the case of a manual grinding, two relaxation rates were observed, corresponding to the ones of $LaPO_4$ and $La_{0.99}Nd_{0.01}PO_4$. In the case of mechanical grinding, only one relaxation time ($T_1 = 20$ s) was observed, with a value equal to the one of the 0.5% doped sample as obtained by the solution

route. This indicates that the planetary mill mixing achieved an homogeneous distribution of the Nd^{3+} ions in the matrix, while the manual mixing did not.

^{31}P MAS NMR relaxation were also performed in Gd doped $LaPO_4$ and in (Gd, Nd) codoped $LaPO_4$. Table 1 compares the ^{31}P relaxation times in Gd doped and Nd doped $LaPO_4$ in the low doping range (from 0 to 1%). Gd appears much more efficient than Nd for enhancing the ^{31}P relaxation. This is related to the slow electronic relaxation rates of the $L = 0$ Gd^{3+} ion as compared to thoses of the $L \neq 0$ Nd^{3+} ion. Measurements of the electronic relaxation rates in both Gd and Nd doped $LaPO_4$ are reported in section 3.3 to characterize this effect. A quantitative relation between nuclear and electronic relaxation rates is worked out in section 4.3.

Table 2 gives the ^{31}P relaxation times in MAS (15 kHz) conditions for four samples doped with both neodymium and gadolinium ions. The Gd concentration was kept constant and equal at 5‰, whereas the Nd concentration was varied from 0 to 7.5‰. The introduction of a small quantity of neodymium into Gd doped $LaPO_4$ significantly enhances the nuclear relaxation, with T_1 decreasing from 3.7 s without Nd to 1.5 s for 7.5‰ Nd doping. The increase of the relaxation cannot be explained by the relaxation directly induced by the Nd^{3+} ions, which is much slower, as shown by the data in Table 1 (24 s and 6 s at 0.5% and 1% Nd doping level, respectively). This effect will be discussed in section 4.4 in relation with the electronic relaxation measurements in codoped (Gd, Nd) samples presented in section 3.3.3.

As compared to static conditions, MAS provides a better resolution and a better signal to noise ratio, but it presents the drawback to disturb the relaxation process by weakening the nuclear dipolar interaction, which insures a common spin temperature through nuclear spin diffusion. In the very dilute doping range, the MAS nuclear relaxation should reflect the spatial distribution of the paramagnetic centers with the initial recovery of the magnetization raising as $t^{D/6}$, with D being the fractal dimension of the network on which the paramagnetic ions are distributed [30,31,32]. In the present case, where the network is a regular 3D lattice, this would give a $t^{1/2}$ law. However, in the moderately dilute regime (1‰ to 1%) which is in interest in the present study, the range of distances between nuclei and paramagnetic centers is not large enough to observe the scaling law. The MAS relaxation is a complicated sum of the individual relaxation profiles of the nuclei located at different distances from the paramagnetic centers. Thus, relaxation measurements were also performed in static conditions where the nuclear spin diffusion is not inhibited by MAS rotation. Figure 7 displays the variation of the ^{31}P relaxation rate both in static and MAS (15 kHz) conditions in the 0-1% Nd doping range. The variation with the doping level is linear, with the MAS relaxation rate

being 1.6 times lower than the static one, in accordance with the weakening of the nuclear spin diffusion mechanism by MAS rotation. At higher concentration, the MAS and static relaxation become equal, reflecting the fact that the direct relaxation to paramagnetic ions overcome the relaxation mediated by nuclear spin diffusion at sufficiently high doping range. Table 1 compares the ^{31}P relaxation rate in Gd-doped $LaPO_4$ and Nd-doped $LaPO_4$ in static and MAS (15 kHz) conditions in the low concentration range (0-1%). Again the MAS T_1 is longer than the static one, and T_1 is shorter in Gd-doped than in Nd-doped $LaPO_4$. The relaxation in the undoped sample is due to uncontrolled paramagnetic impurities contained in the nitrate and phosphate precursors or in the crucibles used for the thermal annealing, as shown by the difference between static and MAS relaxation times. Their concentration is equivalent to 34 ppm of Gd^{3+}.

3.3. ESR

3.3.1. Gd doped $LaPO_4$

The ESR spectrum of Gd doped $LaPO_4$ was observed from 4 K up to room temperature. It presents a quite complicated structure due to the high spin fundamental state ($^8S_{7/2}$) of the Gd^{3+} ion and to the low symmetry of the crystal structure [33]. It does not change too much with temperature (Figure 8), which means that the linewidth is not controlled by the spin-lattice relaxation that is expected to be strongly temperature-dependent.

On the contrary, the spectrum landscape exhibits a substantial smoothing as the Gd concentration is increased. This is shown in Figure 2-SI that displays a detail of the ESR line at 20 K and 30 dB for three Gd concentrations, 1‰, 1% and 5%. The broadening is determined by fitting the high concentration spectra by the convolution of the 1‰ spectrum with Lorentzian lines. The best agreement was obtained by using a line broadening of 2.5 mT for 1%, and 16 mT for 5%. The broadening arises from the dipolar coupling between the Gd^{3+} spins. The dipolar broadening field B_D can be estimated using the expression for dilute spins [34]:

$$B_D = \frac{\mu_0}{4\pi}\,\frac{4\pi^2}{9}\,\hbar\gamma_{\mathrm{Gd}}\,\sqrt{S(S+1)}\;\;n_{\mathrm{Gd}}$$

where $S = 7/2$, and n_{Gd} is the Gd ion density, which is given by $n_{\mathrm{Gd}} = N\,x\,/\,V$, where $N = 4$ is the number of Gd sites per unit cell, and $V = 0.306$ nm^3 is the volume of the unit cell. Using this approximate expression, one gets 0.4 mT, 4 mT and 21 mT for x = 1‰, 1% and 5%, respectively, in rough agreement with the empirical estimation.

The saturation curves were obtained by recording the ESR line as a function of the microwave power. Figure 9 displays the variation of the ESR intensity at two static fields as a function of the microwave magnetic field, B_1, for $LaPO_4$:Gd 1‰. Only a few temperatures are presented for the sake of the clarity of the drawing. The saturation curves were fitted using [35]:

$$S(B_1) = S_0 \frac{B_1}{1 + (B_1 / B_s)^2} \qquad (1)$$

where the saturation field B_s is related to the longitudinal and transverse relaxation rates (ρ_1 and ρ_2) and times (τ_1 and τ_2) by: $\gamma_{Gd} B_s = \sqrt{\rho_1 \rho_2} = 1/\sqrt{\tau_1 \tau_2}$.

Figure 10 displays the variation of $\sqrt{\rho_1 \rho_2}$ as a function of temperature. The determination of $\sqrt{\rho_1 \rho_2}$ was possible up to room temperature for Gd 1‰. It is limited to 150 K for Gd 5‰ (not shown), 50 K for Gd 1%, and to 20 K for Gd 5%, since for higher temperatures the saturation curves remain in the linear initial regime up to the highest available microwave power. The low field (0.13 T) relaxation is about 50% faster than the high field (0.24 T) one. This is expected, since both the spin lattice relaxation rate (ρ_1) and the distance from the free electron g value are governed by the spin-orbit coupling. Thus, the more shifted the measurement field from the g = 2 field (0.34 T in our case), the greater the relaxation rate. For the four concentrations, the thermal variation of $\sqrt{\rho_1 \rho_2}$ appears linear in the available temperature range. The coefficients of the linear variation are given in Table 1-SI. One may suggest that the variation with the concentration arises from the ρ_2 contribution, while the variation with temperature comes from the ρ_1 contribution. The latter could correspond to a high temperature Raman process giving rise to a T^2 temperature dependence and thus, to give a linear temperature variation for $\sqrt{\rho_1 \rho_2}$.

3.3.2. Nd doped $LaPO_4$

The ESR spectrum of Nd doped $LaPO_4$ was only observed at low temperature (T < 40 K) due to the very fast spin relaxation of the Nd^{3+} ion at higher temperature. The splitting of the fundamental $^4I_{9/2}$ multiplet by the crystal field reduces the spin system to an effective spin $S = 1/2$ with an anisotropic g factor. Figure 11a shows that the whole ESR spectrum can be quite well-fitted using: $g_x = 3.52$, $g_y = 2.95$ and $g_z = 0.98$. In addition to its five spinless isotopes, the Nd nucleus has two isotopes with spin 7/2, ^{143}Nd (abundance 12.2%) and ^{145}Nd (abundance 8.3%), whose Lande factor are $g_{143} = -0.31$ and $g_{145} = -0.19$, respectively. Since the Zeeman and the hyperfine interactions have the same symmetry, the hyperfine tensor **A** should be colinear to the **g** tensor [36]: $A_x/g_x = A_y/g_y = A_z/g_z$. Thus, the hyperfine tensors for the two spin 7/2 nuclei only depend on a unique scalar parameter A:

$\mathbf{A}_{143} = g_{143}\, A\, \mathbf{g}$ and $\mathbf{A}_{145} = g_{145}\, A\, \mathbf{g}$. Figure 11b shows that the satellite lines are reasonably well-fitted using A = 1027 MHz.

The Nd ESR line undergoes a considerable broadening with increasing temperature as shown by Figure 3-SIa. The broadening was estimated by fitting the experimental lines by the convolution of the low temperature line (8 K) with Lorentzian lines of different linewidths. As an example, Figure 3-SIb shows that the 20 K line can be accurately fitted using a 3 mT Lorentzian broadening. Table 2-SI gives the broadening field B_2 at the different temperatures, together with the corresponding transverse relaxation rate (ρ_2) and time (τ_2): $\rho_2 = 1/\tau_2 = \gamma_{\mathrm{Nd}}\, B_2$. A broadening was also observed as a function of the Nd concentration. However, it is negligible with respect to the temperature broadening, except at very low temperature.

The saturation of the signal intensity as a function of the microwave power was only observed at the lowest temperatures. The saturation field B_s obtained by fitting the saturation curves, as well as the related products $\sqrt{\rho_1 \rho_2}$ and $\sqrt{\tau_1 \tau_2}$ are given in Table 3-SI up to 12 K. At 15 K, the slight departure from a linear variation of the saturation curves is not sufficient to determine a reliable value of B_s. The values given in Table 3-SI were obtained by considering the central peak of the structure (g_y) around 0.23 T (see Figure 3-SIa). Measurements made at the 0.195 T peak position (g_x) led to relaxation rates (times) about 30% faster (shorter).

Both Tables 2-SI and 3-SI exhibit very fast variations of the relaxation rates (times) with temperature. Moreover, when put together on the same drawing (Figure 12), the thermal variations of ρ_2 and $\sqrt{\rho_1 \rho_2}$ appear to be on the same line in a log-log plot. This highlights the equality of the longitudinal and transverse relaxation rates or times (τ_1 and τ_2) in Nd-doped $LaPO_4$. This is not really surprising: because of the strong spin-orbit coupling of the Nd^{3+} ion ($L \neq 0$), the fast spin-lattice relaxation mechanism predominates over the other transverse relaxation processes, in contrast to the situation in Gd doped $LaPO_4$. The sharp power low temperature dependence $\rho_1 = \rho_2 \sim T^x$ with x of the order of 5 to 6 points out a low temperature Raman process involving a multiplet with small or moderate splitting [37].

3.3.3. Gd-Nd codoped $LaPO_4$

The ESR spectra of Gd-Nd codoped $LaPO_4$ samples are the superimposition of the ESR spectrum of $LaPO_4$:Gd and $LaPO_4$:Nd in the 0-40 K temperature range, where the Nd^{3+} signal can be observed. Above 40 K, the ESR spectra are the same as the ones obtained for Gd doped $LaPO_4$. Table 2 gives the values of the square root of the product of the longitudinal and transverse relaxation times, $\sqrt{\tau_1 \tau_2}$, at two temperatures for codoped samples with a fixed

Gd^{3+} concentration (0.5%) and a Nd^{3+} concentration varying from 0 to 0.75%. The measurements were performed at the position of the main peak of the Gd ESR spectrum (0.24 T), as explained in section 3.3.1. They entirely reflect the relaxation of the Gd^{3+} ion since the intensity of the Nd^{3+} spectrum is quite low at this field, and more importantly, the Nd^{3+} relaxation is much faster than the Gd^{3+} one. The results show that the addition of a small amount of Nd^{3+} ions significantly enhances the Gd^{3+} relaxation rates.

4. Discussion

4.1. Homogeneity of the magnetic rare-earth admixture in $LaPO_4$

We show that the evolution of the reciprocal nuclear relaxation time ($1/T_1$) varies linearly as a function of the doping concentration in the 0-10 at.% range in the case of doped $LaPO_4$ samples made by coprecipitation (Figure 5). The linearity indicates a homogeneous admixture of the magnetic rare-earth ions in the $LaPO_4$ matrix. Indeed, the presence of rare-earth clusters would lead to a departure from the linearity, as already reported by Sen *et al.* [15,16].

For samples made through the solid-state route, the relaxation time depends on the nature of the grinding (Figure 6). For manual grinding, a bi-exponential decay was observed, proving the non-homogeneity of the Nd distribution in the sample, *i.e.* a short T_1 attributed to the P nuclei in the vicinity of the Nd clusters, and a long T_1 corresponding to the P nuclei located in the domains with low Nd concentration. In the case of the mechano-synthesis with a planetary mill, only one relaxation time is obtained, similar to what is observed for the samples made by coprecipitation. In this case, Nd^{3+} ions are homogeneously distributed in the matrix.

We thus conclude that the distribution of the doping ions depends on the synthesis method and our approach is adapted to study optimized process of synthesis. For the solid-state route, a key parameter is an intimate grinding of the reagents to favor the homogeneity of the doping ion distribution by convection or ionic diffusion. If the mixing is not sufficient, clusters are present in the matrix unless a high temperature annealing is applied for a long duration time.

4.2. Accuracy of the determination of the magnetic rare-earth doping concentration

The linear evolution of the ^{31}P relaxation rate as a function of the Nd^{3+} in the 0-10 at.% range, as well as the agreement with the ICP/MS analysis, indicates that the actual magnetic rare-earth concentration in $LaPO_4$ corresponds to the nominal one in this range.

Based on the measurement of nuclear relaxation time, one can determine the content of Nd^{3+} ions in $LaPO_4$ monazite, as long as the relaxation time is close to exponential *i.e.* as long as the rare-earth incorporation is homogeneous. It is particularly interesting for low doping level (0 to 1 at.%), where other methods, such as the ICP/MS or the variation of the unit cell parameter measured by X-Ray diffraction, appear to be not sensitive enough. This is highlighted in Figure 7, which shows a well-defined linear variation of the relaxation rates, whereas the variation of the cell parameter is somewhat chaotic due to the inaccuracy of the measurement. Thus the measurement of the nuclear relaxation appears as a promising method to determine effective low doping levels (< 1 at.%) in the cases where the admixture of the dopant is not guaranteed by a structural isomorphism. At these weak doping levels, we can estimate the accuracy on the concentration measurement to 0.1 at.%.

4.3. Understanding the nuclear relaxation mechanisms

The theory of the nuclear relaxation by dilute magnetic ions is outlined in the appendix. The distance b_2, which characterizes the nuclear spin diffusion barrier, can be calculated from Eqs. (A2) and (A3). It is worth 0.1 and 0.15 nm in Nd and Gd doped $LaPO_4$, respectively, for ^{31}P at room temperature in a magnetic field of 8.5 T. The distance b_1, which characterizes the efficiency of the nuclear spin diffusion with respect to the direct relaxation process, cannot be calculated exactly since it depends on the value of the electronic relaxation time through Eq. (A1). However, one can work out a maximum value for it by noting that the quantity $\omega_I \tau_1 / (1 + \omega_I^2 \tau_1^2)$ is always smaller than 1/2. It turns out that b_1 is smaller than b_2 for both Nd and Gd doped $LaPO_4$ in our experimental conditions (300 K, 8.5 T). The ^{31}P relaxation is thus in the fast spin diffusion regime for weakly doped $LaPO_4$. This is due to the 100% abundance and the high gyromagnetic factor of the ^{31}P isotope.

Then, one can attempt an estimate of the electronic relaxation time from the nuclear relaxation measurements using Eqs. (A1) and (A4). The density of paramagnetic ions is related to the doping concentration, x, by $n_J = N x / V$, where $N = 4$ is the number of rare-earth site per unit cell, and $V = 0.306$ nm^3 is the volume of the unit cell. Thus, Eq. (A4) can be rewritten as

$$\frac{1}{T_1} = A \frac{x \, \tau_1}{1 + \omega_I^2 \, \tau_1^2}$$

where the constant A is

$$A = \frac{8\pi}{15}\left(\frac{\mu_0}{4\pi}\right)^2 \frac{N\hbar^2\gamma_I^2\gamma_J^2 J(J+1)}{V\ b_2^3}.$$

It should be remarked that the relationship between the nuclear T_1 and the electronic τ_1 is different in Nd and Gd doped $LaPO_4$. For Nd doped $LaPO_4$, the very short τ_1 implies that $\omega_I \tau_1 << 1$. Thus, the nuclear relaxation rate is proportional to the electronic relaxation time: $1/T_1 = A\,x\,\tau_1$. From the variation of the static $1/T_1$ as a function of x (Figure 7), one obtains $\tau_1 \approx 4.6$ ps. From the ESR experiments, one knows that $\tau_1 \approx \tau_2 \approx 1$ ns at 30 K. The strong power law variation observed at low temperature (Figure 12) cannot be extrapolated up to room temperature, since it would give an unrealistically short relaxation time of the order of a few fs. Instead, the steep low temperature variation should change into a smoother T^2 law characteristic of a high temperature Raman process. Thus, a relaxation time of a few ps seems reasonable and compatible in order of magnitude with the ESR experiments.

On the contrary, the relatively long τ_1 leads to $\omega_I\ \tau_1 >> 1$ for Gd doping. The nuclear and electronic relaxation rates are thus proportional: $1/T_1 = A\,x/(\omega_I^2\,\tau_1)$. From the value of T_1 at $x = 1$‰ in static conditions (Table 1), one deduces $\tau_1 = 42$ ns. This value is of the same order of magnitude as $(\tau_1\,\tau_2)^{1/2} \approx 50$ to 100 ns, determined by ESR at room temperature for the same 1‰ Gd-doped $LaPO_4$ sample (Figure 10a). However, as τ_1 is expected to be longer than τ_2, the $\tau_1 = 42$ ns value deduced from NMR measurement seems to short as compared to the value that can be infered from the ESR experiments. Nevertheless, one should notice that NMR and ESR experiments are performed at quite different magnetic field (8.5 T for NMR and 0 to 0.8 T for ESR). This probably explains the difference between the NMR and ESR estimates of the electronic relaxation time.

4.4 Codoping effect

Table 2 shows that both the ^{31}P nuclear relaxation time and the Gd^{3+} electronic relaxation time decrease when small amounts of Nd^{3+} are added in samples containing a fixed concentration of Gd^{3+}. Due to the non-vanishing orbital moment, the Nd^{3+} ions are much more coupled to the lattice phonon bath than the Gd^{3+} ions, and thus they relax much more rapidly. In codoped samples, the dipolar coupling between the Gd^{3+} and Nd^{3+} magnetic moments provide an additional path of relaxation for the Gd^{3+} electronic spins *via* the rapidly relaxing Nd^{3+} ions. This causes the speed-up of the Gd^{3+} electronic relaxation. In turn, this gives rise to an increase of the nuclear ^{31}P relaxation rate since nuclear and electronic relaxation rates are proportional in Gd doped $LaPO_4$, as explained in the preceding section.

This result may be of great interest in the field of magnetic resonance imaging (MRI), where contrast agents with fast relaxing properties are sorely searched. By adding a small amount of rapidly relaxing rare earth ions (such as Nd^{3+}) in particles containing Gd^{3+}, the most commonly used contrast agent, one can enhance the electronic Gd^{3+} relaxation, and consequently the nuclear relaxation of the surrounding nuclei (usually protons) [38]. By adjusting the Nd concentration, it would be possible to fit the relation $\omega_I \tau_1 \approx 1$ that optimizes the nuclear relaxation process (Eq. A1).

5. Conclusion

In monazite $LaPO_4$ samples doped with x at.% Nd^{3+} (or Gd^{3+}) (x varying from 0 to 10) made by coprecipitation followed by a thermal annealing at 1000 °C, the recovery of the nuclear ^{31}P magnetization follows a nearly exponential law, attesting for a homogeneous distribution of the Nd^{3+} (resp. Gd^{3+}) doping ion in the $LaPO_4$ network. The solid-state NMR measurements performed in MAS and static conditions allow to get the value of the ^{31}P relaxation time T_1 as a function of the Nd (or Gd) concentration. We show that $1/T_1$ varies linearly with the Nd (or Gd) doping content in the 0-10 at.% range, allowing an accurate determination of the magnetic ion concentration at low doping level. Below 1%, this measurement appears to be much more accurate to determine the doping concentration than the usual method based on the variations of the cell parameters as obtained by X-ray diffraction techniques. Such a study can be extended to $LaPO_4$ doped with other paramagnetic ions such as Er^{3+}, Yb^{3+} or Ce^{3+}.

In addition, the homogeneity of the doping ion distribution can be characterized by comparing the measurement of the nuclear relaxation in samples synthesized in different conditions. Whereas the doping appears always homogeneous in the synthesis by the solution route, we show that the mixing step is essential to ensure a homogeneous distribution of the doping ions in the case of a solid-state synthesis consisting in mixing oxide precursors followed by a high temperature annealing.

Finally, the association of NMR and ESR relaxation measurements permits to understand the nuclear relaxation mechanisms in both Nd and Gd doped $LaPO_4$, and shows that the efficiency of Gd as relaxing agent in MRI experiments can be improved by Nd-Gd codoping.

6. Acknowledgment

Alain Louis-Joseph, Mathis Plapp and Jean-Pierre Boilot (PMC) are warmly thanked for valuable discussions. The authors also thank François Beuneu (LSI) and Jürgen von Bardeleben (INSP) for using their ESR spectrometers and for their valuable advice.

Appendix: the nuclear relaxation induced by dilute magnetic ions

For a nuclear spin $I = 1/2$ such as ^{31}P, the relaxation rate due to the dipolar coupling with a magnetic ion of momentum J at a fixed distance r can be expressed as [39]

$$\frac{1}{T_1} = \left(\frac{\mu_0}{4\pi}\right)^2 \frac{J(J+1)}{15} \frac{\hbar^2 \gamma_I^2 \gamma_J^2}{r^6} \left[\frac{6\tau_1}{1+\omega_I^2 \tau_1^2} + \frac{14\tau_2}{1+\omega_J^2 \tau_2^2}\right]$$

where γ_I (γ_J) and ω_I (ω_J) are the nuclear (electronic) gyromagnetic factors and Larmor frequencies, respectively, and τ_1 and τ_2 are the longitudinal and transverse electronic relaxation times. Since ω_J is much larger than ω_I, the second contribution can be neglected in most cases, and the relaxation rate is rewritten as $1/T_1 = C / r^6$ with

$$C = \frac{2}{5}\left(\frac{\mu_0}{4\pi}\right)^2 J(J+1)\,\hbar^2 \gamma_I^2 \gamma_J^2 \frac{\tau_1}{1+\omega_I^2 \tau_1^2}. \qquad \text{(A1)}$$

However, the relaxation by direct coupling competes with the one mediated through the nuclear spin diffusion, whose radius grows as the square root of time: $r = (D\,t)^{1/2}$, where D is the nuclear spin diffusion coefficient [40,41]. As the direct relaxation radius grows as $r = (C\,t)^{1/6}$, one can defines a distance $b_1 = (C/D)^{1/4}$, beyond which it is overpassed by the relaxation through spin diffusion.

Moreover, it exists a distance b_2 below which the shift of the nuclear resonance frequency due to their dipolar coupling with the electronic magnetic moment makes the nuclear spin diffusion ineffective. It can be defined by [42]

$$\gamma_I \left.\frac{d\,h_J(r)}{d\,r}\right|_{r=b_2} a_0 = \Delta\omega.$$

In this expression, $\Delta\omega$ is the homonuclear dipolar linewidth, a_0 the mean distance between neighboring nuclear spins, and $h_J(r)$ is the electronic dipolar magnetic field experienced by the nuclear spin at the distance r. As the latter is given by $h_J(r) = (\mu_0/4\pi)(\hbar\,\gamma_J/r^3) < J^Z >$, this leads to

$$b_2 = a_0 \left(\frac{\mu_0}{4\pi} \frac{3\hbar\gamma_I\gamma_J}{\Delta\omega} < J^Z >\right)^{1/4}. \qquad \text{(A2)}$$

Except to very low temperature where the electronic τ_1 may become longer than the nuclear T_2, the mean value of the electronic kinetic moment is given by the Curie law:

$$< J^Z > = \frac{\hbar\,\gamma_J B_0}{k_B T} \frac{J(J+1)}{3} \qquad \text{(A3)}$$

where B_0 is the magnetic field, and T the temperature.

In the region where the relaxation through nuclear spin diffusion is both (i) more efficient than the direct relaxation ($r > b_1$) and (ii) not inhibited by the spreading of the resonance frequencies ($r > b_2$), the nuclear spin diffusion establishes a common spin

temperature, and the recovery of the nuclear magnetization is exponential with a relaxation rate equal to the mean of the individual rates:

$$\frac{1}{T_1} = n_J\, C \iiint_{r>b} \frac{d^3\mathbf{r}}{r^6} = \frac{4\pi n_J}{3}\,\frac{C}{b^3} = \frac{C}{R^3 b^3}$$

where $b = \max(b_1, b_2)$, n_J is the density of magnetic ions, and $R = (4\,\pi\, n_J/\,3)^{-1/3}$ is the range of influence of each magnetic ion. The expression of the mean relaxation rate is the same as the one for individual relaxation with an effective distance that is equal to the harmonic mean of the distances, b and R, that limit the spin diffusion domain around the magnetic ion. The result is, however, quite different depending whether b_1 is larger or smaller than b_2. In the first case, one obtains: $1/T_1^{SSD} = C/(R\,b_1)^3 = C^{1/4}\,D^{3/4}/R^3$ [39]. This is the regime of Slow Spin Diffusion (*SSD*), where the spin diffusion coefficient D appears explicitly in the expression of the relaxation rate. On the opposite, for $b_1 < b_2$, one obtains the Fast Spin Diffusion regime (*FSD*) [41,42]

$$\frac{1}{T_1^{FSD}} = \frac{C}{b_2^3 R^3} = \frac{4\pi n_J}{3}\frac{C}{b_2^3}\ . \qquad \text{(A4)}$$

In the near surrounding of the magnetic ions ($r < b$), the nuclear spin diffusion is either inhibited ($r < b_2$), inefficient ($r < b_1$) or both. It cannot achieve a common spin temperature. Thus, one has to sum the individual relaxation profiles and the whole relaxation is not exponential. However, this contribution is generally hardly visible since (i) it corresponds to a weak fraction of the nuclei in the dilute regime, (ii) the resonance frequency of the involved nuclei is frequently shifted out of the NMR line, and (iii) it gives rise to a very fast relaxation that can be missed by the measuring process.

[1] I. Y. Jung, Y. Cho, S. G. Lee, S. H. Sohn, D. K. Kim, D. K. Lee, Y. M. Kweon, *Appl. Phys. Lett.*, 2005, **87**, 191908.

[2] S. Ye, F. Xiao, Y. X. Pan, Y. Y. Ma, Q. Y. Zhang, *Materials Science and Engineering: R.: Reports*, 2010, **71**, 1.

[3] J. Brgoch, C. K. H. Borg, K. A. Denault, A. Mikhailovsky, S. P. Benbaars, R. Seshadri, *Inorg. Chem.*, 2013, **52**, 8010.

[4] A. Huignard, T. Gacoin, J. P. Boilot, *Chem. Mater.*, 2000, **12**, 1090.

[5] S. B. Alaparthi, L. Lu, Y. Tian, Y. Mao, *Mater. Res. Bull.*, 2014, **49**, 114.

[6] N. George, A. J. Pell, G. Dantelle, K. Page, A. Llobet, M. Balasubramanian, G. Pintacuda, B. F. Chmelka, R. Seshadri, *Chem. Mater.*, 2013, **25**, 3979.

[7] P. Barua, E. H. Sekiya, K. Saito, A. J. Ikushima, *J. Non-Cryst. Solids*, 2008, **354**, 4760.

[8] L. Vegard, *Z. Phys. A*, 1921, **5**, 17.

[9] A. Lyberis, G. Patriarche, P. Gredin, D. Vivien, M. Mortier, *J. Eur. Ceram. Soc.*, 2011, **31**, 1619.

[10] N. Ollier, J. L. Doualan, V. Pukhkaya, T. Charpentier, R. Moncorgé, S. Sen, *J. Non-Cryst. Solids*, 2011, **357**, 1037.

[11] O. Guillot-Noël, P. Goldner, P. Higel, D. Gourier, *J. Phys Condens. Matter*, 2004, **16**, R1.

[12] G. Dantelle, M. Mortier, P. Goldner, D. Vivien, *J. Phys Condens. Matter*, 2006, **18**, 7905.

[13] A. C. Palke, J. F. Stebbins, *Am. Mineral.*, 2011, **96**, 1343.

[14] A. C. Palke, J. F. Stebbins, L. A. Boatner, *Inorg. Chem.*, 2013, **52**, 12605.

[15] S. Sen, J. F. Stebbins, *Phys. Rev. B: Condens. Matter Mater. Phys.*, 1994, **50**, 822.

[16] S. Sen, J. F. Stebbins, *J. Non-Cryst. Solids*, 1995, **188**, 54.

[17] E. M. Levin, J. P. Heremans, M. G. Kanatzidis, K. Schmidt-Rohr, *Phys. Rev. B: Condens. Matter Mater. Phys.*, 2013, **88**, 115211.

[18] H. Meyssamy, K. Riwotzki, A. Kornowski, S. Naused, M. Haase, *Adv. Mater.*, 1999, **11**, 840.

[19] K. Riwotzki, H. Meyssamy, A. Kornowski, M. Haase, *J. Phys. Chem. B*, 2000, **104**, 2824.

[20] V. Buissette, M. Moreau, T. Gacoin, J. P. Boilot, J. Y. Chane-Ching, T. Lemercier, *Chem. Mater.*, 2004, **16**, 3767.

[21] D. Bregiroux, F. Audubert, T. Charpentier, D. Sakellariou, D. Bernache-Assolant, *Solid State Sci.*, 2007, **9**, 432.

[22] http://jp-minerals.org/vesta/en/ .

[23] J. Rodríguez-Carvajal, *Phys. B (Amsterdam, Neth.)*, 1993, **192**, 55.

[24] J. Rodríguez-Carvajal, http://www.ill.eu/sites/fullprof/index.html .

[25] S. Stoll, A. Schweiger, *J. Magn. Reson.*, 2006, **178**, 42.

[26] S. Lucas, E. Champion, D. Bregiroux, D. Bernache-Assolant, F. Audubert, *J. Solid State Chem.*, 2004, **177**, 1302.

[27] D. Tse, S. R. Hartmann, *Phys. Rev. Lett.*, 1968, **21**, 511.

[28] J. F. Stebbins, K. E. Kelsey, *Phys. Chem. Chem. Phys.*, 2009, **11**, 6906.

[29] E. M. Levin, B. A. Cook, K. Ahn, M. G. Kanatzidis, K. Schmidt-Rohr, *Phys. Rev. B: Condens. Matter Mater. Phys.*, 2009, **80**, 115211.

[30] F. Devreux, J. P. Boilot, F. Chaput, B. Sapoval, *Phys. Rev. Lett.*, 1990, **65**, 614.

[31] A. Hodroj, P. Simon, P. Florian, M. H. Chopinet, Y. Vaills, *J. Am. Ceram. Soc.*, 2013, **96**, 2454.

[32] S. J. Widgeon, S. Sen, G. Mera, E. Ionescu, R. Riedel, A. Navrotsky, *Chem. Mater.*, 2010, **22**, 6221.

[33] M. Rappaz, M. M. Abraham, J. O. Ramey, L. A. Boatner, *Phys. Rev. B: Condens. Matter Mater. Phys.*, 1981, **23,** 1012.

[34] A. Abragam, in *The Principles of Nuclear Magnetism*, ed. E. C. Bullard, N. F. Mott, D. H. Wilkinson, Oxford University Press, London, 1961, ch. IV, pp. 125-128.

[35] A. Abragam, B. Bleaney, in *Electron Paramagnetic Resonance of Transitions Ions*, ed. W. Marshall and D. H. Wilkinson, Oxford University Press, London, 1970, chap. 2, pp. 115-119.

[36] A. Abragam, B. Bleaney, in *Electron Paramagnetic Resonance of Transitions Ions*, ed. W. Marshall and D. H. Wilkinson, Oxford University Press, London, 1970, chap. 1, pp. 33-39.

[37] A. Abragam, B. Bleaney, in *Electron Paramagnetic Resonance of Transitions Ions*, ed. W. Marshall and D. H. Wilkinson, Oxford University Press, London, 1970, chap. 1, pp. 60-74.

[38] H. B. Na, I. C. Song, T. Hyeon, *Adv. Mater.*, 2009, **21**, 2133.

[39] A. Abragam, in *The Principles of Nuclear Magnetism*, ed. E. C. Bullard, N. F. Mott, D. H. Wilkinson, Oxford University Press, London, 1961, chap. IX, pp. 378-386.

[40] A. Abragam, in *The Principles of Nuclear Magnetism*, ed. E. C. Bullard, N. F. Mott, D. H. Wilkinson, Oxford University Press, London, 1961, chap. V, pp. 136-144.

[41] M. Goldmann, in *Spin Temperature and Nuclear Magnetic Resonance in Solids*, Oxford University Press, London, 1970, pp. 65-67.

[42] I. P. Goudemond, J. M. Keartland, M. J. R. Hoch, G. A. Saunders, *Phys. Rev. B: Condens. Matter Mater. Phys.*, 2001, **63**, 054413.

Tables

x (%)	MAS T_1		static T_1	
	Gd	Nd	Gd	Nd
0	600	600	245	245
0.1	21	100	8.5	55
0.5	3.7	24	0.84	17
1	0.46	6.3	0.28	8.9

Table 1. Spin-lattice relaxation time (T_1 in s) of $La_{1-x}Gd_xPO_4$ and of $La_{1-x}Nd_xPO_4$ for x varying from 0 to 1% in MAS (15 kHz) and static conditions.

y (%)	MAS T_1 (s) 300 K	$\sqrt{\tau_1 \tau_2}$ (ns) 4.6 K	$\sqrt{\tau_1 \tau_2}$ (ns) 20 K
0	3.7	294	155
0.25	2.1	70	51
0.5	1.6	57	43
0.75	1.5	48	28

Table 2. The ^{31}P nuclear spin-lattice relaxation time at room temperature and the square root of the product of the longitudinal and transverse electronic relaxation times $\sqrt{\tau_1 \tau_2}$ at two temperatures in $La_{0.995-y}Gd_{0.005}Nd_yPO_4$ for different y values. $\sqrt{\tau_1 \tau_2}$ is related to the saturation field B_s by $\sqrt{\tau_1 \tau_2} = 1/(\gamma_{Gd} B_s)$, with B_s being measured by fitting the variation of the intensity of the ESR signal at 0.24 T as a function of the microwave power using Eq. (1).

Figure captions

Figure 1. Crystallographic view of the monazite phase of $REPO_4$ obtained with Vesta software [22]. The PO_4^{3-} tetrahedrons are colored in grey, the RE atoms in light green and the oxygen atoms in red.

Figure 2. Variation of the three cell parameters as a function of the Nd^{3+} content for $La_{1-x}Nd_xPO_4$ ($0 \leq x \leq 1$) obtained by coprecipitation. The dashed lines represent the Vegard's law as calculated from the JCPDF files (01-083-0651 for $LaPO_4$ and 00-025-1065 for $NdPO_4$).

Figure 3. a): ^{31}P MAS NMR spectra of $La_{0.99}Nd_{0.01}PO_4$ obtained by coprecipitation of $La(NO_3)_3$, $Nd(NO_3)_3$ and TPP with a nitrate to TPP ratio equal to 1:3 and an annealing temperature of 1000 °C. The repetition delay is equal to $5*T_1$.
b): zoom of the MAS NMR spectrum of $La_{0.99}Nd_{0.01}PO_4$ resulting from a thermal annealing at 1000 °C, highlighting the presence of the paramagnetic peaks resulting from the interaction between the P nuclei and their Nd paramagnetic neighbor, thanks to a repetition delay of 50 ms. The paramagnetic peaks are labelled according to Palke *et al.* [13].

Figure 4. ^{31}P MAS NMR spectra of $La_{1-x}Nd_xPO_4$ at $\omega_r = 15$ kHz, with x varying from 0% ($LaPO_4$) to 100% ($NdPO_4$), with a repetition delay of $5*T_1$ for each sample. The spinning-rotation bands of the $NdPO_4$ spectrum are labelled by a star (*).

Figure 5. Variation of the relaxation rate ($1/T_1$) at $\omega_r = 15$ kHz of ^{31}P atoms in $La_{1-x}Nd_xPO_4$ as a function of the neodymium content with x varying from 0 to 100%. The inset highlights the linear variation for x between 0 and 10%.

Figure 6. ^{31}P magnetization recovery for two samples obtained through the solid-state route by mixing $LaPO_4$ and $La_{0.99}Nd_{0.01}PO_4$ either manually in a mortar (full square, bottom scale) or using a planetary mill (empty square, upper scale).

Figure 7. Left scale: the ^{31}P relaxation rate in Nd doped $LaPO_4$ in the low doping range in static conditions (red circles) and under MAS conditions at 15 kHz (red squares). Right scale: the cell parameter a (blue triangles) as measured by XRD in the same doping range.

Figure 8. The normalized ESR spectra of $La_{0.999}Gd_{0.001}PO_4$ at 20 K and 290 K with the same (non saturating) microwave power (30 dB). In green the simulation made by the software Easyspin [25] using $g = 1.994$, $D = 2491$ MHz and $E = 407$ MHz [33].

Figure 9. Saturation curves of $La_{0.999}Gd_{0.001}PO_4$ at different temperatures for $B_0 = 0.13$ T (a) and $B_0 = 0.24$ T (b). The dashed lines are the data fit using Eq. (1).

Figure 10. Square root of the product of the electronic longitudinal and transverse relaxation rates $\sqrt{\rho_1 \rho_2}$ as a function of temperature for two different static fields, 0.13 T (red circles) and 0.24 T (blue squares) and for three Gd^{3+} concentrations: 1‰ (a), 1% (b), 5% (c). $\sqrt{\rho_1 \rho_2}$ were obtained by fitting the saturation curves using Eq. (1).

Figure 11. ESR line of $La_{0.99}Nd_{0.01}PO_4$ at 7 K and 30 dB. (a) the whole spectrum and (b) the detail of the low field side amplifying the hyperfine satellites of the main line. The lines were fitted (in green) with the software EasySpin [25] using the following parameters: $g_x = 3.52$, $g_y = 2.95$, $g_z = 0.98$, $A = 1027$ MHz.

Figure 12. Temperature variation of the relaxation rates in $LaPO_4$:Nd 1‰. The transverse relaxation rate ρ_2 (red square) was obtained by fitting the broadening of the linewidth in the 12-30 K range (see Fig. 3-SIb and Table 2-SI). The square roots of the product of the longitudinal and transverse relaxation rates $\sqrt{\rho_1 \rho_2}$ were obtained by saturation in the 4-12 K range at two measuring fields, 0.19 T (blue cross) and 0.23 T (blue circle) (see Table 3-SI).

Figures

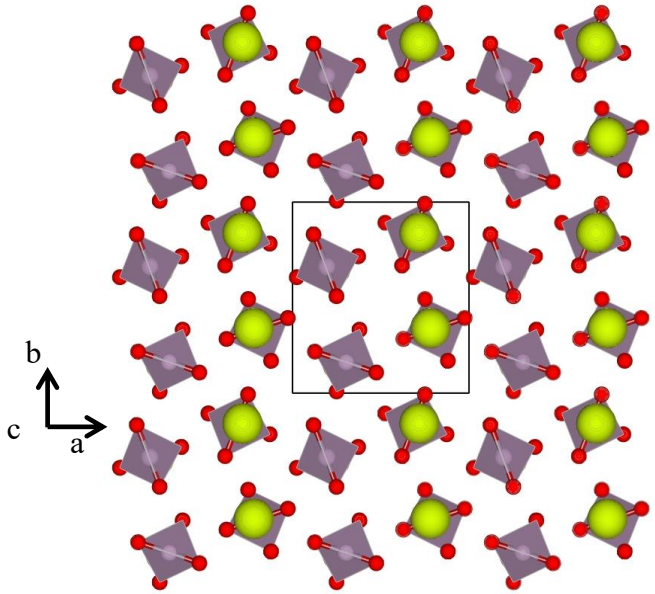

Figure 1. Crystallographic view of the monazite phase of $REPO_4$ obtained with Vesta software [22]. The PO_4^{3-} tetrahedrons are colored in grey, the RE atoms in light green and the oxygen atoms in red.

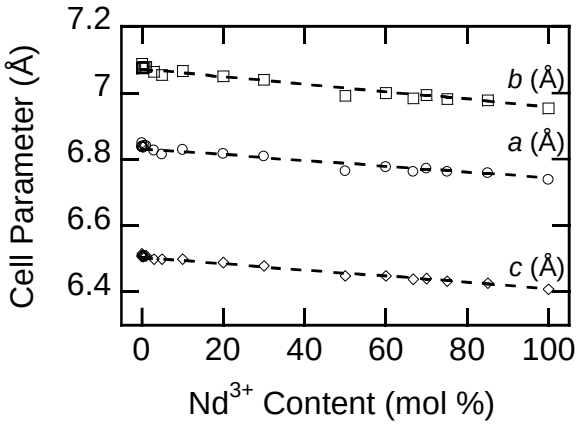

Figure 2. Variation of the three cell parameters as a function of the Nd^{3+} content for $La_{1-x}Nd_xPO_4$ ($0 \leq x \leq 1$) obtained by coprecipitation. The dashed lines represent the Vegard's law as calculated from the JCPDF files (01-083-0651 for $LaPO_4$ and 00-025-1065 for $NdPO_4$).

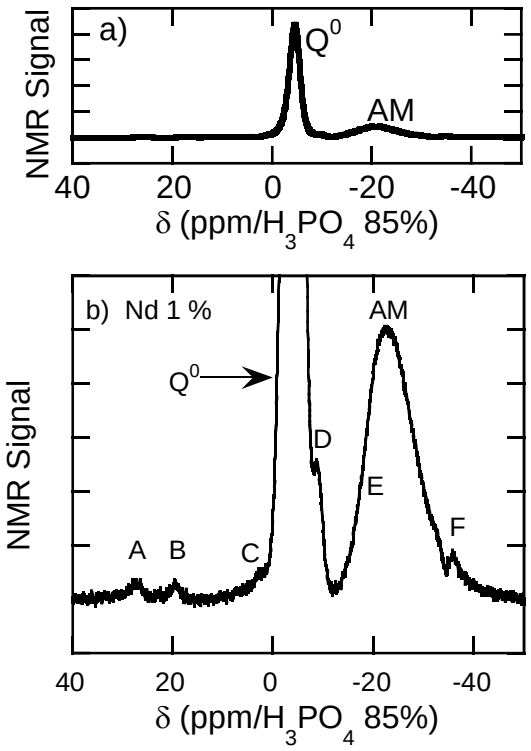

Figure 3. a): ^{31}P MAS NMR spectra of $La_{0.99}Nd_{0.01}PO_4$ obtained by coprecipitation of $La(NO_3)_3$, $Nd(NO_3)_3$ and TPP with a nitrate to TPP ratio equal to 1:3 and an annealing temperature of 1000 °C. The repetition delay is equal to $5*T_1$.

b): zoom of the MAS NMR spectrum of $La_{0.99}Nd_{0.01}PO_4$ resulting from a thermal annealing at 1000 °C, highlighting the presence of the paramagnetic peaks resulting from the interaction between the P nuclei and their Nd paramagnetic neighbor, thanks to a repetition delay of 50 ms. The paramagnetic peaks are labelled according to Palke *et al.* [13].

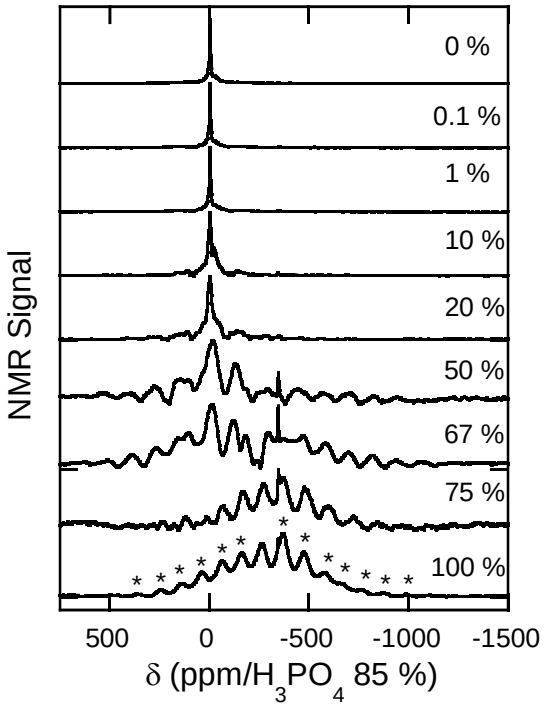

Figure 4. ^{31}P MAS NMR spectra of $La_{1-x}Nd_xPO_4$ at $\omega_r = 15$ kHz, with x varying from 0% ($LaPO_4$) to 100% ($NdPO_4$), with a repetition delay of $5*T_1$ for each sample. The spinning-rotation bands of the $NdPO_4$ spectrum are labelled by a star (*).

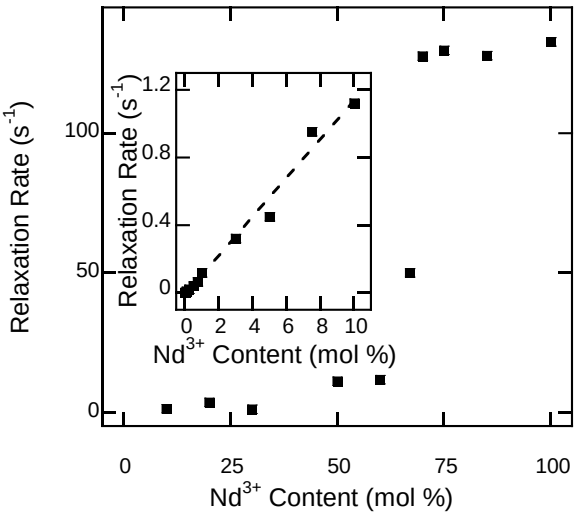

Figure 5. Variation of the relaxation rate ($1/T_1$) at ω_r = 15 kHz of ^{31}P atoms in $La_{1-x}Nd_xPO_4$ as a function of the neodymium content with x varying from 0 to 100%. The inset highlights the linear variation for x between 0 and 10%.

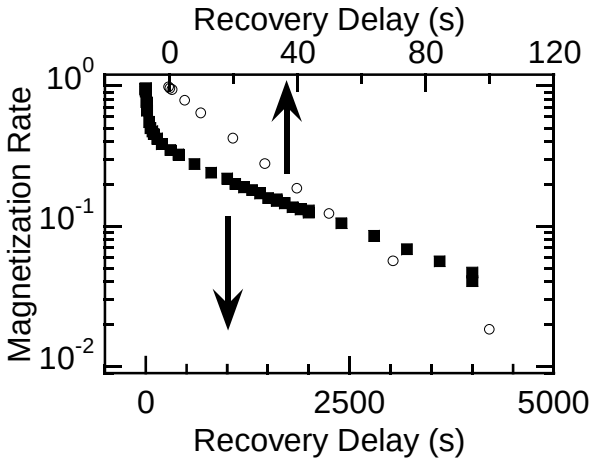

Figure 6. ^{31}P magnetization recovery for two samples obtained through the solid-state route by mixing $LaPO_4$ and $La_{0.99}Nd_{0.01}PO_4$ either manually in a mortar (full square, bottom scale) or using a planetary mill (empty circle, upper scale).

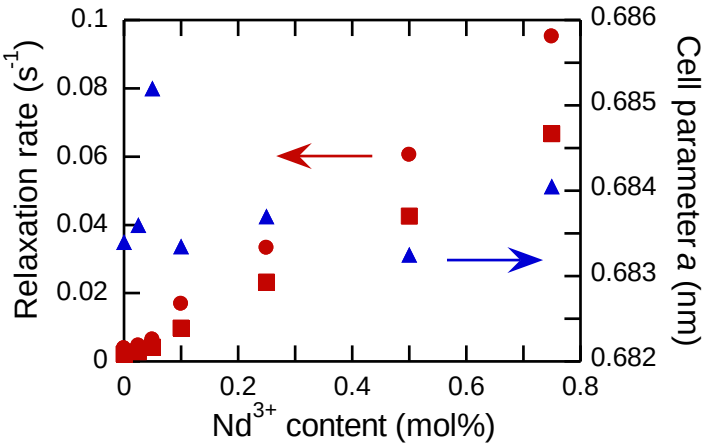

Figure 7. Left scale: the ^{31}P relaxation rate in Nd doped $LaPO_4$ in the low doping range in static conditions (red circles) and under MAS conditions at 15 kHz (red squares). Right scale: the cell parameter *a* (blue triangles) as measured by XRD in the same doping range.

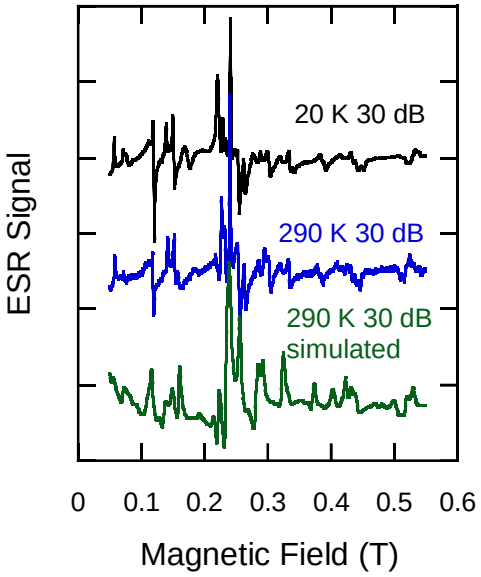

Figure 8. The normalized ESR spectra of $La_{0.999}Gd_{0.001}PO_4$ at 20 K and 290 K with the same (non saturating) microwave power (30 dB). In green the simulation made by the software Easyspin [25] using $g = 1.994$, $D = 2491$ MHz and $E = 407$ MHz [33].

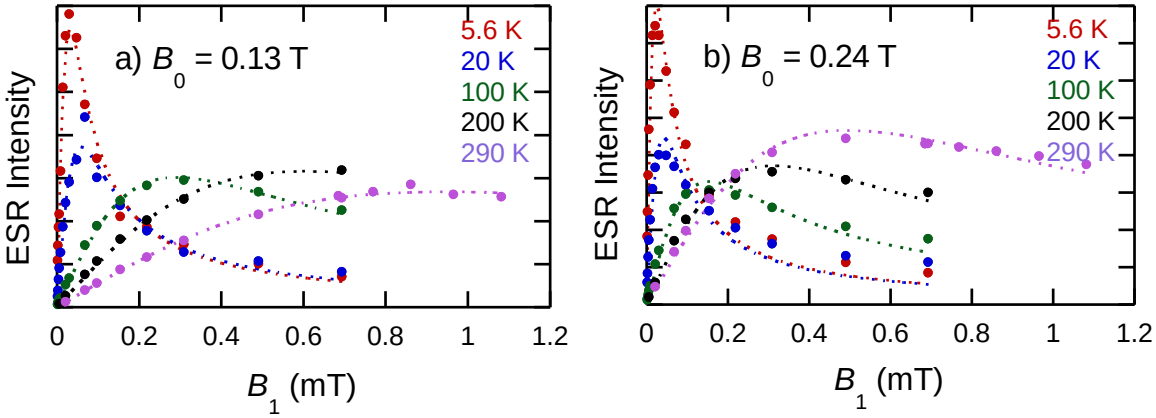

Figure 9. Saturation curves of $La_{0.999}Gd_{0.001}PO_4$ at different temperatures for B_0 = 0.13 T (a) and B_0 = 0.24 T (b). The dashed lines are the data fit using Eq. (1).

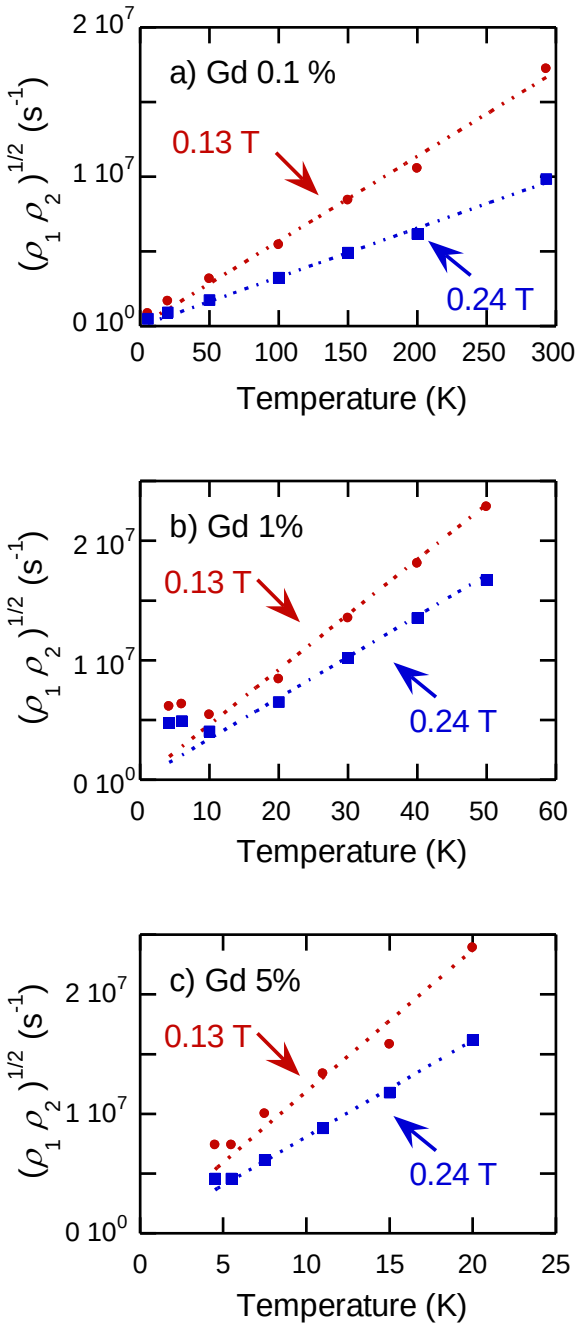

Figure 10. Square root of the product of the electronic longitudinal and transverse relaxation rates $\sqrt{\rho_1 \rho_2}$ as a function of temperature for two different static fields, 0.13 T (red circles) and 0.24 T (blue squares) and for three Gd^{3+} concentrations: 1‰ (a), 1% (b), 5% (c). $\sqrt{\rho_1 \rho_2}$ were obtained by fitting the saturation curves using Eq. (1).

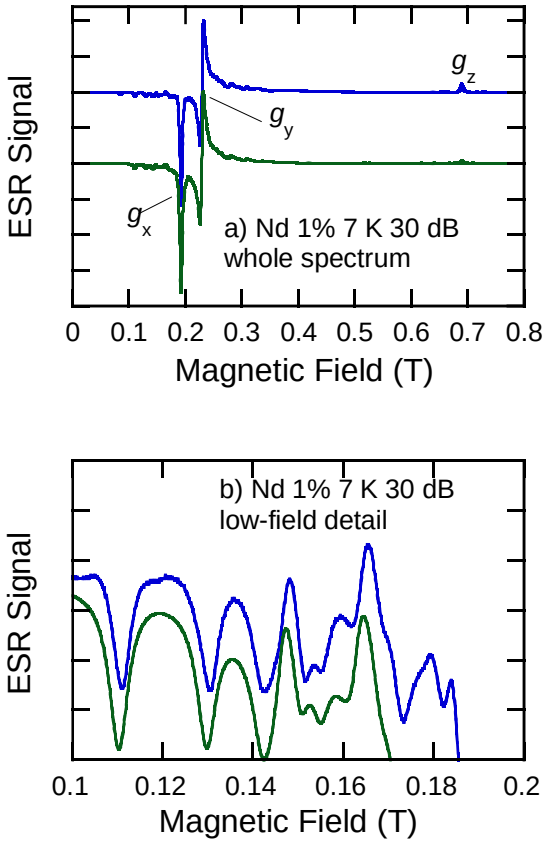

Figure 11. ESR line of $La_{0.99}Nd_{0.01}PO_4$ at 7 K and 30 dB. (a) the whole spectrum and (b) the detail of the low field side amplifying the hyperfine satellites of the main line. The lines were fitted (in green) with the software EasySpin [25] using the following parameters: $g_x = 3.52$, $g_y = 2.95$, $g_z = 0.98$, $A = 1027$ MHz.

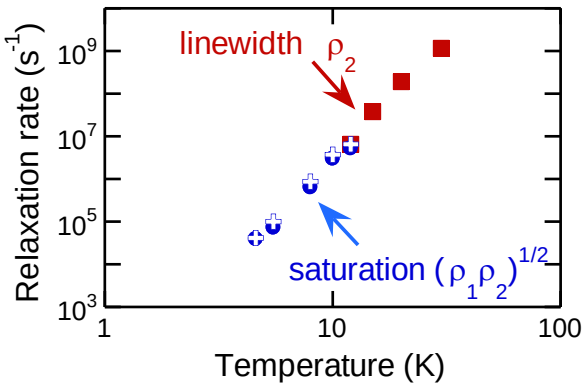

Figure 12. Temperature variation of the relaxation rates in $LaPO_4$:Nd 1‰. The transverse relaxation rate ρ_2 (red square) was obtained by fitting the broadening of the linewidth in the 12-30 K range (see Fig. 3-SIb and Table 2-SI). The square roots of the product of the longitudinal and transverse relaxation rates $\sqrt{\rho_1 \rho_2}$ were obtained by saturation in the 4-12 K range at two measuring fields, 0.19 T (blue cross) and 0.23 T (blue circle) (see Table 3-SI).